

Mutual Coupling in RIS-Aided Communication: Model Training and Experimental Validation

Pinjun Zheng, Ruiqi Wang, Atif Shamim, *Fellow, IEEE*, and Tareq Y. Al-Naffouri, *Senior Member, IEEE*

Abstract—This paper investigates the mutual coupling in reconfigurable intelligent surface (RIS)-aided communication. Despite the existence of several mutual coupling-aware models for RIS-aided communication, the absence of experimental validation remains a notable gap. To fill this void, this work delves into the recently proposed mutual coupling-aware communication model based on scattering matrices. Utilizing a fabricated 1-bit quasi-passive RIS prototype operating in the mmWave band, we first propose a novel model training approach based on a single 3D full-wave simulation of the RIS radiation pattern, enabling the estimation of the scattering matrix among RIS unit cells. Subsequently, the trained model is validated via both full-wave simulations and experimental measurements on the real RIS prototype. Compared with the conventional communication model without accounting for mutual coupling in RIS, the utilized mutual coupling-aware model, incorporating trained scattering parameters, showcases a more accurate prediction performance. Benchmarked against the full-wave simulated RIS radiation pattern, the trained model can reduce the prediction error by up to 10.6%. Meanwhile, the S-parameter between the Tx and Rx antennas is measured, validating that the trained model exhibits a closer alignment with the experimental measurements. Such results affirm the correctness of the adopted model and the effectiveness of the proposed model training method.

Index Terms—reconfigurable intelligent surface, mutual coupling, wireless communication, mmWave, 5G/6G.

I. INTRODUCTION

Standing as a groundbreaking technique in modern wireless communication systems, reconfigurable intelligent surfaces (RISs) represent a revolutionary paradigm for the smart electromagnetics (EM) wave control [1]–[4]. These surfaces, composed of an array of programmable reflective or refractive unit cells, empower real-time adjustments to the radio environment. Leveraging advanced metamaterials and signal processing techniques, RIS enables precise modulation of the phase, amplitude, and polarization of EM waves. Such adaptability promises to significantly benefit wireless applications including communication, sensing, localization, and mapping [5]–[9]. With the advent of dense-integrated RISs such as holographic RIS [10], the phenomenon of mutual coupling emerges as a critical consideration with profound implications for the performance of RIS-assisted communications [1]. Mutual coupling refers to the interaction between adjacent RIS unit cells, wherein the EM fields generated by one unit cell influence the behavior of its neighboring unit cells. This inter-element coupling effect can significantly

impact the overall functionality and effectiveness of an RIS deployment, especially in scenarios involving high amplitude gains or varying operational frequencies. Therefore, understanding and mitigating the impact of mutual coupling is essential in optimizing the performance of RIS systems.

A. Prior Work and Motivation

RIS-aided communication has been extensively studied in recent years owing to its substantial potential in extending communication coverage [11], enhancing signal reception [12], and improving energy efficiency [13]. To date, numerous novel signal processing techniques have been developed to support RIS-aided communications. The authors of [14] proposed an atomic norm minimization-based channel estimation algorithm for RIS-aided multiple-input multiple-output (MIMO) systems in the mmWave band. Novel beamforming techniques have been explored for various purposes such as sum-rate maximization [15], localization accuracy improvement [16], and transmission security enhancement [17].

Recent investigations into mutual coupling within RIS have resulted in notable advancements in modeling and performance optimization. Notably, existing mutual coupling-aware communication models can be categorized into two types: impedance matrix-based models and scattering matrix-based models. In the impedance matrix-based approach, the first effort can be found in [18], where an EM-compliant and mutual coupling-aware communication model is proposed by adopting the mutual impedance analysis among RIS unit cells. The authors of [19] further provided a refined mutual impedance evaluation approach in a closed-form manner by introducing a linear dipole assumption. This model has proven effective in guiding RIS configuration, facilitating applications such as end-to-end received power maximization in single-input-single-output (SISO) systems [20] and sum-rate optimization in multi-user interference MIMO channels [21]. On the other hand, the scattering matrix-based model, rooted in microwave network theory, was initially explored by the authors of [22] through a scattering parameter network analysis. Subsequently, the authors of [23] proposed a scattering matrix-based mutual coupling-aware communication model. Importantly, the derivation in [23] establishes the equivalence between the impedance matrix-based and scattering matrix-based communication models, allowing seamless conversion between the two representations.

While there exist several established mutual coupling-aware communication models, the absence of experimental validation for these models remains a critical gap. Due to the passive

The authors are with the Electrical and Computer Engineering Program, Division of Computer, Electrical and Mathematical Sciences and Engineering (CEMSE), King Abdullah University of Science and Technology (KAUST), Thuwal, 23955-6900, Kingdom of Saudi Arabia.

reflective nature of RIS, the accurate scattering parameters or mutual impedances between its unit cells cannot be directly acquired through simulation or measurement. To the best of our knowledge, there is no literature reporting a practical assessment of the coupling effect in any real RIS hardware so far. The lack of realistic evaluations for the scattering parameters or mutual impedances between RIS unit cells makes the validation of the emerging mutual coupling-aware communication models in actual hardware more challenging. Motivated by these considerations, this paper aims to develop a practical approach to attain an accurate estimation of mutual coupling in an actual RIS prototype, and then, validate the accuracy of the estimated model via both full-wave simulation and experimental measurement.

B. Main Contributions

The main contributions of this paper are summarized as follows.

Model Training: Although several models have pointed out how the mutual coupling (either in the form of impedance matrix or scattering matrix) plays a role in the wireless communication channel.¹ The realistic evaluation of these impedance or scattering matrices is still missing. By only considering the coupling between adjacent RIS unit cells and neglecting very weak coupling effects beyond the distance of two unit cells, we parameterize the scattering matrix of the RIS into a finite set of scattering parameters. Based on this parameterized approximation, we design a training approach to estimate these scattering parameters based on a single 3D full-wave EM simulation of the radiation pattern of the designed RIS prototype. The simulated RIS radiation pattern accurately captures the 3D EM behavior including mutual coupling, thus we can estimate these scattering parameters by optimizing their fitness to the simulated pattern. These results yield a realistic evaluation of the mutual coupling in the utilized RIS prototype and thus enable the validation of the mutual coupling-aware model based on the estimated scattering matrix.

Simulation Validation: The mutual coupling-aware communication model with the trained scattering parameters is validated through the full-wave simulation. First, we perform the full-wave simulations of 3 different RIS radiation patterns by varying the position of the Tx antenna. In the meantime, the theoretical predictions of these radiation patterns are obtained using the mutual coupling-aware model (with the trained scattering parameters) and the conventional mutual coupling-unaware model, respectively. Benchmarked against the simulated radiation patterns, the trained model exhibits superior accuracy compared to the conventional model without accounting for mutual coupling, validating the precision of the trained model.

Experimental Validation: To further confirm the trained model, experimental validation is also carried out in this work.

¹In this work, our investigation is based on the scattering matrix-based model which describes the relationship between the transmitted and received voltages, as it keeps better compatibility with the commonly adopted communication model without mutual coupling.

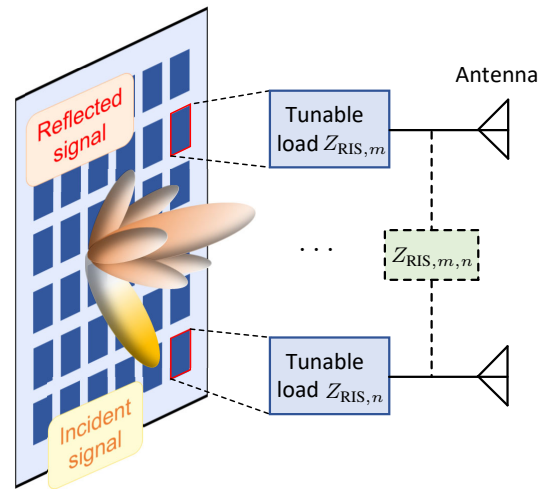


Fig. 1. Conceptual architecture of an RIS.

The experimental measurements are conducted on a 1-bit RIS prototype reported in [24], designed to operate in the mmWave frequency range spanning from 22.7 to 30.5 GHz with a quasi-passive reflecting property. We use two horn antennas to respectively transmit and receive EM signals, and measure the S-parameter between the two horn antennas through a vector network analyzer. Afterward, this S-parameter is predicted by the trained model and the conventional model, respectively. The comparisons over different setups demonstrate that the trained model can predict the S-parameter closer to the real measurement, revealing both the correctness of the adopted mutual coupling-aware communication model and the effectiveness of the proposed scattering parameters training approach.

The paper is organized as follows. Section II introduces the fundamentals of RIS hardware. Section III recaps the RIS-aided communication models, including both the conventional mutual coupling-unaware model and the recently proposed mutual coupling-aware model based on scattering matrices. Leveraging a 3D full-wave simulation of the RIS radiation pattern, a training approach for the scattering parameters among RIS unit cells is proposed in Section IV. Based on the trained model, the simulation validation and the experimental validation are conducted in Section V and Section VI, respectively. Finally, the conclusions of the paper are drawn in Section VII.

II. FUNDAMENTALS OF RIS HARDWARE

A. Functional Principle of RIS

An RIS is a planar surface that consists of an array of scattering unit cells, each of which can impose an independent phase shift, and possibly an amplitude gain, on the incident EM waves. Fig. 1 depicts a conceptual structure of the RIS. As illustrated, each RIS unit cell is equivalently comprised of an antenna and a functional circuit with tunable load $Z_{\text{RIS},m}$ [22], [25], [26], where m denotes the index of the unit cell. By carefully adjusting the tunable loads of all the unit cells, the

desired phase shifts (and amplitude gains) can be achieved thus the reradiated EM waves can be beamformed toward specified directions. As shown in Fig. 1, different RIS unit cells, e.g., $Z_{\text{RIS},m}$ and $Z_{\text{RIS},n}$, can be further connected through a reconfigurable impedance $Z_{\text{RIS},m,n}$, which is referred to as the beyond diagonal RIS or group/fully-connected RIS as recently proposed in [23], [27]. For clarification, this work uses the classical RIS with independent unit cells, which is also called the single-connected RIS.

Each unit cell of the RIS can be treated as a 1-port network. The voltage waves impinging on the port (denoted as V_{in}) and reflected from the port (denoted as V_{re}) are related through the reflection coefficient Θ as

$$V_{\text{re}} = \Theta V_{\text{in}}. \quad (1)$$

That is, a phase shift $\angle\Theta$ and an amplitude gain $|\Theta|$ are imposed on the incident EM wave. The reflection coefficient Θ is determined by the load impedance Z_{RIS} of the RIS unit cell through the relationship [22], [28]

$$\Theta = \frac{Z_{\text{RIS}} - Z_0}{Z_{\text{RIS}} + Z_0}, \quad (2)$$

where Z_0 is the reference impedance (or the characteristic impedance) and usually $Z_0 = 50 \Omega$. Depending on the real part of the load impedance Z_{RIS} , various types of RIS can be distinguished as follows.

- $\text{Re}(Z_{\text{RIS}}) > 0$: This yields an amplitude gain $|\Theta| < 1$ and is the case of the most real hardware of the quasi-passive RIS [24].
- $\text{Re}(Z_{\text{RIS}}) = 0$: This yields a unit-modulus constraint $|\Theta| = 1$ which is widely adopted in the existing theoretical work for simplicity. The unit-modulus reflection coefficient can be realized through a purely reactive RIS load [2], [8], [13], [22], [29].
- $\text{Re}(Z_{\text{RIS}}) < 0$: This yields an amplitude gain $|\Theta| > 1$ which is known as the active RIS [30]. Several technologies can realize a negative resistance. For example, by imposing proper bias voltage, the tunnel diode can work in the negative differential resistance regions thus leading to an active power gain [31].

B. A Fabricated Quasi-Passive RIS Prototype

Based on the functional principle in Section II-A, a practical wideband 1-bit quantized quasi-passive RIS operating at the 5G mmWave band has been designed and fabricated for the verification of the mutual coupling effect. This RIS prototype utilizes a single-connected network architecture [27]. The RIS unit cell design, array synthesis, simulation, and fabricated prototype are demonstrated as follows.

1) *RIS Unit Cell Design*: The detailed design methodology for wideband RIS unit element has been investigated in our previous work [24]. The phase shift and amplitude gain of the designed unit cell (with 0° incidence) when the PIN switch at ON/OFF states are shown in Fig. 2. We can observe reflection amplitude larger than -2.8 dB and phase difference within $180^\circ \pm 20^\circ$ for the bandwidth from 22.7 to 30.5 GHz (fully cover the 5G n257 and n258 bands). For example, at the

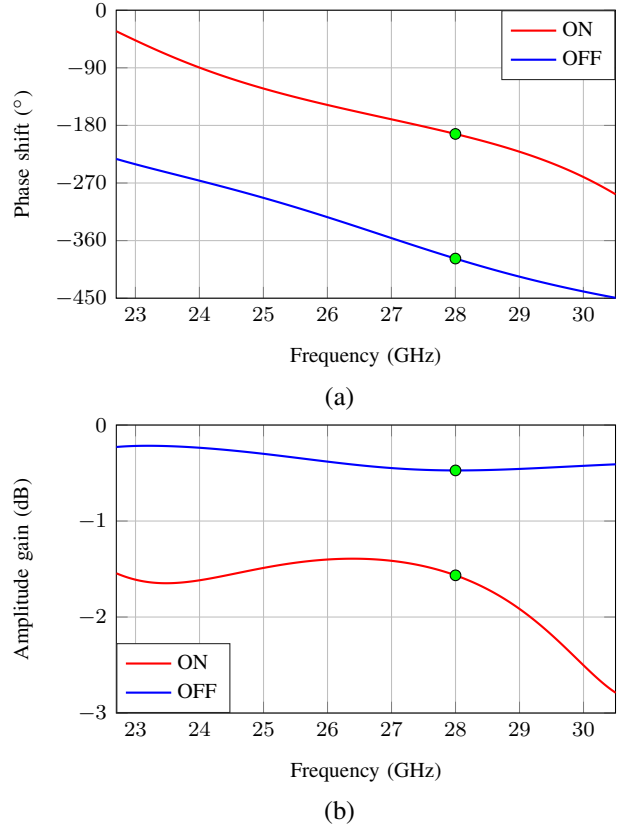


Fig. 2. The designed RIS unit cell performance between ON and OFF states. (a) Phase shift. (b) Amplitude gain.

frequency of 28 GHz (as highlighted in Fig. 2), each RIS unit cell has the phase and amplitude responses as follows.

$$\angle\Theta = \begin{cases} -193.3^\circ & \text{if PIN state} = \text{ON}, \\ -388.1^\circ & \text{if PIN state} = \text{OFF}, \end{cases} \quad (3)$$

$$|\Theta| = \begin{cases} -1.57 \text{ dB} & \text{if PIN state} = \text{ON}, \\ -0.47 \text{ dB} & \text{if PIN state} = \text{OFF}. \end{cases} \quad (4)$$

The designed RIS has a small unit cell size of $0.35\lambda \times 0.35\lambda$ at the center operation frequency of 27.5 GHz. Based on the existing results in the literature, the mutual coupling effect among RIS unit cells becomes severe when the antenna inter-distance is shorter than half-wavelength [20]. Therefore, the designed RIS prototype should have an observable strong mutual coupling between adjacent RIS antennas, suggesting its suitability for the experimental validation of mutual coupling.

2) *RIS Array Simulation*: Before the fabrication and measurement, the radiation performance of the designed RIS can be evaluated through the full-wave simulation based on the finite element method (FEM), which captures precise EM characteristics including mutual coupling. For this design, the RIS is composed of 400 unit elements in a 20×20 configuration, as demonstrated in Fig. 3. The simulation of the RIS with 400 elements and an incident horn antenna has almost reached the computation limit of the workstation with 256G RAM. Fig. 4 illustrates a sample of the simulated 3D radiation pattern along with the RIS and in a polar plot. It should be noted

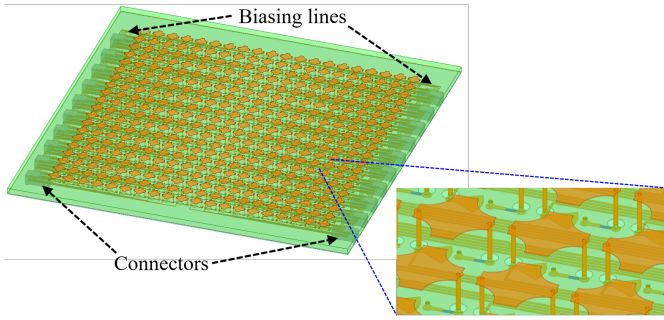


Fig. 3. The practical RIS design.

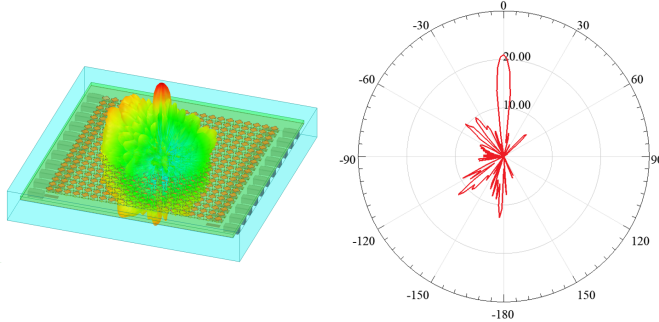


Fig. 4. The simulated radiation patterns of the designed RIS with array configuration for 30° illumination and a desired 0° -reflection beamforming at 27.5 GHz.

that different radiation patterns can be achieved by varying the signal incident angle, RIS beamforming, and the distance between RIS and the incident horn antenna. However, the mutual coupling parameters, as will be shown in Section III-B, are independent of these system setups and only depend on the physical layout of the RIS antennas. Therefore, the simulated radiation patterns under different system setups can be utilized to train and test the model parameters of the mutual coupling, since it is unable to measure them directly.

3) *Fabricated Prototype*: Typically, a completely functional RIS design is comprised of a periodic structure with magnitude/phase modulation and a digital circuit for the array pattern generation and control. In this work, the designed control circuits and the packaged RIS prototype are shown in Fig. 5. Specifically, the designed circuit board links with a microcontroller unit (MCU) WROOM-32 module that can compute the array patterns, as illustrated in Fig. 5-(a). The circuit is designed with 8-bit phase registers (74HC595D) and PMOS to bias the PIN switches, as shown in Fig. 5-(b). When the output of the phase register is at the high voltage level, the PIN switch is turned on, thus the RIS unit cell, as demonstrated in Fig. 5-(c), is in the ON state. Otherwise, the corresponding unit cell is in the OFF state. The phase distribution map of the RIS can be visualized through an LED array in the back of the control circuit. Fig. 5-(d) demonstrates the overall fabricated RIS prototype, including the RIS array, control circuit board, connectors, and flexible printed circuit (FPC), which are packaged together through 3D-printed mechanical supports using a Raise3D Pro2 printer with polylactic acid filaments. Note that the function of FPC here is to connect the

RIS array with the whole designed circuits inside the package.

III. RIS-AIDED COMMUNICATION MODELS

As a foundation of the subsequent analyses, this section reviews the RIS-aided communication models, including both the conventional model that does not account for RIS mutual coupling [32] and the recently proposed mutual coupling-aware communication model [23]. Consider a RIS-aided MIMO communication with a M_T -antenna transmitter, a M_R -antenna receiver, and a RIS with N unit cells. Let $\mathbf{v}_R \in \mathbb{C}^{M_R \times 1}$ and $\mathbf{v}_T \in \mathbb{C}^{M_T \times 1}$ denote the total voltages at the receiver and the transmitter, respectively. The wireless channel is represented by the channel matrix $\mathbf{H} \in \mathbb{C}^{M_R \times M_T}$, which builds the connection between \mathbf{v}_R and \mathbf{v}_T as

$$\mathbf{v}_R = \mathbf{H}\mathbf{v}_T. \quad (5)$$

A. Conventional Channel Model without Mutual Coupling

A commonly adopted RIS-aided communication channel \mathbf{H} can be expressed as [2], [8], [13], [26], [32], [33]

$$\mathbf{H} = \mathbf{H}_{RT} + \mathbf{H}_{RI}\mathbf{\Theta}\mathbf{H}_{IT}, \quad (6)$$

where $\mathbf{H}_{RT} \in \mathbb{C}^{M_R \times M_T}$ denotes the Tx-Rx channel, $\mathbf{H}_{IT} \in \mathbb{C}^{N \times M_T}$ denotes the Tx-RIS channel, $\mathbf{H}_{RI} \in \mathbb{C}^{M_R \times N}$ denotes the RIS-Rx channel, and $\mathbf{\Theta} \in \mathbb{C}^{N \times N}$ is the RIS reflection matrix. Here, $\mathbf{\Theta}$ is a diagonal matrix whose diagonal entries are given by (2). The expressions of these channel matrices \mathbf{H}_{RT} , \mathbf{H}_{RI} , and \mathbf{H}_{IT} will be specified in Section VI.

Although channel model (6) is widely utilized, it disregards the interactions between adjacent RIS antennas, i.e., the mutual coupling effect. In general, the mutual coupling in an antenna array can be reasonably ignored if the antenna spacing is large enough (e.g., larger than the half wavelength [20], [34]). Nonetheless, the significance of mutual coupling becomes increasingly pronounced with the advent of techniques like holographic MIMO with extremely compact antenna integration, yielding an antenna spacing much shorter than the half wavelength. Therefore, the mutual coupling-aware communication models are required.

B. Mutual Coupling-Aware Channel Model

To account for the mutual coupling effect in RIS-aided communication, several novel communication models have been recently proposed. These models can be categorized into two types: the impedance matrix (Z-parameters)-based model [18] and the scattering matrix (S-parameters)-based model [22]. It should be noted that based on microwave network theory, these two types of models are essentially equivalent and can be seamlessly converted to each other. Such a relationship has been thoroughly analyzed in [23] and [35].

In this work, we adopt the scattering matrix-based communication model, which was first reported in [23, Eq. (5)]² as

$$\mathbf{H} = \mathbf{H}_{RT} + \mathbf{H}_{RI}(\mathbf{\Theta}^{-1} - \mathbf{S})^{-1}\mathbf{H}_{IT}, \quad (7)$$

²Note that the transmission scattering matrices \mathbf{S}_{RT} , \mathbf{S}_{RI} , and \mathbf{S}_{IT} in [23, Eq. (5)] are equivalently the channel matrices from the transmitter to receiver, from the transmitter to RIS, and from the RIS to receiver, respectively. This relationship has been proved by [22, Eq. (35)–(39)].

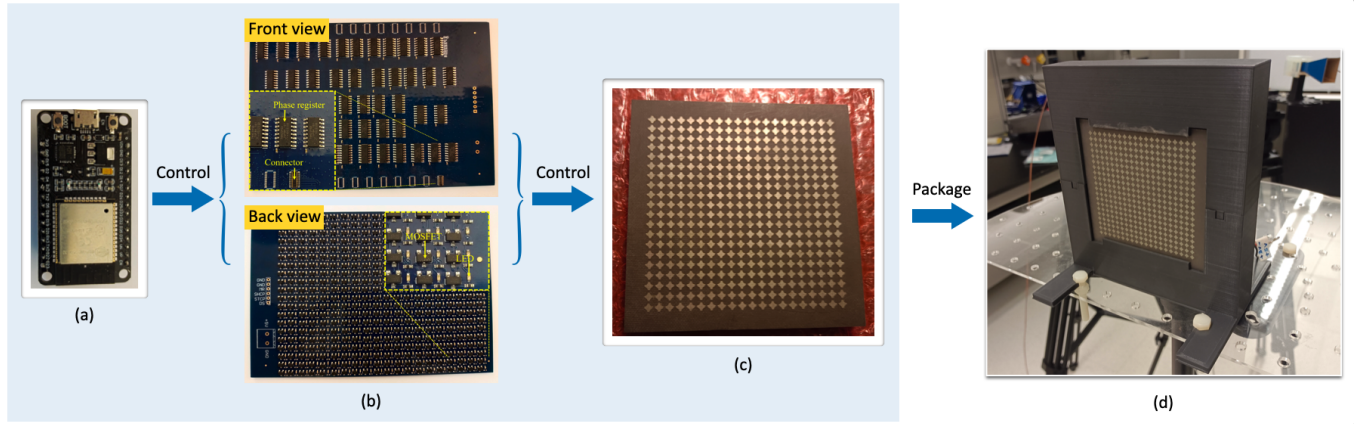


Fig. 5. The fabricated RIS prototype. (a) WROOM-32 module. (b) The designed circuits for the RIS patterns control. (c) The array of the reflective unit cells. (d) The fabricated RIS prototype with integrated control circuits in a package.

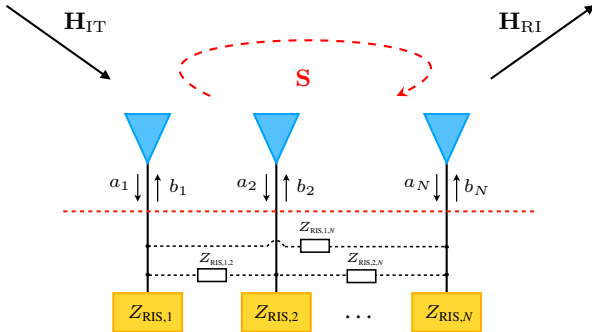


Fig. 6. Network representation of a typical RIS-aided wireless communication system, where the RIS can be treated as an N -port network. The mutual coupling effect is characterized by the scattering matrix \mathbf{S} among RIS antennas.

where $\mathbf{S} \in \mathbb{C}^{N \times N}$ denotes the scattering matrix of the RIS antenna network and thus characterizes the mutual coupling. Specifically, the entry S_{ij} in \mathbf{S} is the S-parameter between the i -th antenna and the j -th antenna on the RIS, which indicates the voltage wave measured at the i -th antenna when a unit voltage wave is driven at the j -th antenna [28]. By reciprocity, we have $S_{ij} = S_{ji}$ thus \mathbf{S} is a symmetric matrix. Additionally, the diagonal entry S_{ii} denotes the self-scattering of the i -th antenna. This model (7) can also be found in, e.g., [35, Eq. (8)] or [36, Eq. (8)].

Basically, model (7) can be derived based on the microwave network analysis. Fig. 6 shows a network representation of a RIS. Let $\mathbf{a} = [a_1, a_2, \dots, a_N]^T \in \mathbb{C}^{N \times 1}$ and $\mathbf{b} = [b_1, b_2, \dots, b_N]^T \in \mathbb{C}^{N \times 1}$ denote the voltage waves that impinge on and reflect from the RIS, respectively. Following the derivation in [23] and [22], the network in Fig. 6 can be examined in two perspectives: (i) If we treat \mathbf{a} as input and \mathbf{b} as output, we have $\mathbf{b} = \mathbf{\Theta}\mathbf{a}$; (ii) If we treat \mathbf{b} as input and \mathbf{a} as output, we have $\mathbf{a} = \mathbf{H}_{IT}\mathbf{v}_T + \mathbf{S}\mathbf{b}$.³ Here, \mathbf{S} represents the

³Strictly, this relationship is obtained under the assumptions that the source impedance at the transmitter, the load impedance at the receiver, and the antenna array at the transmitter are all independent and perfectly matched. The detailed derivation can be found in [23].

process of how the signal \mathbf{b} , emitted from the antenna array, is scattered and then returns to be received by the antenna array itself, which is known as the *mutual coupling* phenomenon. In addition, it can be observed that when $\mathbf{S} = \mathbf{0}$, i.e., in the case without mutual coupling in RIS, model (7) is reduced to the conventional model (6).

IV. SCATTERING MODEL TRAINING

Now, we have two communication models (6) and (7). However, as can be observed in (7), to utilize this mutual coupling-aware model, we still need to determine the scattering matrix \mathbf{S} . Since our RIS prototype only reflects EM waves passively, this scattering matrix \mathbf{S} cannot be measured or simulated directly. Hence, in this paper, we first propose a model training method that can estimate matrix \mathbf{S} based on a single 3D full-wave simulation of the RIS radiation pattern. Then, based on the estimated scattering matrix $\hat{\mathbf{S}}$, we can evaluate and compare the accuracy of the two communication models. In this section, we first introduce the theoretical calculation of the RIS radiation pattern based on the two communication models. Next, we propose a model training method leveraging such theoretical models and a 3D full-wave simulation of the RIS radiation pattern.

A. Theoretical Radiation Pattern Calculation

Since our measurement facility with horn Tx and Rx antennas form a SISO setup, we now present the calculation of the RIS radiation pattern based on the SISO version of (6) and (7). Aiming to evaluate the RIS mutual coupling, we focus on the Tx-RIS-Rx channel only and block the Tx-Rx path that is unrelated to RIS.

The radiation pattern refers to a function of the radiation properties of an antenna array as a function of the directional coordinates [37].⁴ By fixing the position of the Tx horn antenna, we can calculate the radiation pattern of the Tx+RIS

⁴Radiation properties include power flux density, radiation intensity, field strength, directivity, phase or polarization. By default, this paper refers to the radiation pattern as the amplitude field pattern.

system. We denote the directional coordinates by the angle-of-departure (AoD) $\boldsymbol{\theta} = [\theta_{\text{az}}, \theta_{\text{el}}]^\top$ departing from the RIS, which consists of an azimuth angle θ_{az} and an elevation angle θ_{el} . In this paper, the elevation angle is defined as the angle between the departure direction and the normal direction of the antenna plane, as utilized in [37].

1) *Radiation Pattern Calculation Based on (6)*: Based on the conventional communication model (6), different RIS unit cells reflect signals independently without interaction. Hence, the (amplitude) radiation pattern in linear scale can be calculated by [38, Eq. (4.7)]

$$E(\boldsymbol{\theta}) = \left| \sum_{n=1}^N \Theta_{n,n} \frac{\cos^{q_e}(\theta_{\text{el}}) \cos^{q_f}(\theta_{\text{T},n})}{\|\mathbf{p}_n - \mathbf{p}_\text{T}\|_2} e^{jk_0(\mathbf{p}_n^\top \mathbf{u}(\boldsymbol{\theta}) - \|\mathbf{p}_n - \mathbf{p}_\text{T}\|_2)} \right|, \quad (8)$$

where $k_0 = 2\pi/\lambda$ is the wavenumber, $\mathbf{p}_n \in \mathbb{R}^3$ denotes the position of the n -th RIS antenna, $\mathbf{p}_\text{T} \in \mathbb{R}^3$ denotes the position of the Tx horn, and $\mathbf{u}(\boldsymbol{\theta})$ denotes the unit directional vector of the AoD $\boldsymbol{\theta}$. All these positions and vectors are expressed in the body coordinate system of the RIS. Here, $\lambda = c/f$ denotes the EM wavelength, where f is the signal frequency and c is the speed of light. Besides, $\theta_{\text{T},n}$ denotes the elevation angle of the AoD from Tx to the n -th RIS unit cell expressed in the coordinate system of the Tx horn, and q_e and q_f is the feed power patterns of the RIS unit cell and the Tx horn antennas, respectively. In addition, $\Theta_{n,n}$ denotes the reflection coefficient of the n -th RIS unit cell, i.e., the n -th diagonal entry of $\boldsymbol{\Theta}$.

We can reform (8) into a more compact form as

$$E(\boldsymbol{\theta}) = |\mathbf{h}_{\text{out}}^\top(\boldsymbol{\theta}) \boldsymbol{\Theta} \mathbf{h}_{\text{in}}|, \quad (9)$$

where the entries in $\mathbf{h}_{\text{in}} \in \mathbb{C}^{N \times 1}$ and $\mathbf{h}_{\text{out}}(\boldsymbol{\theta}) \in \mathbb{C}^{N \times 1}$ are given by

$$h_{\text{in},n} = \frac{\cos^{q_f}(\theta_{\text{T},n})}{\|\mathbf{p}_n - \mathbf{p}_\text{T}\|_2} e^{-jk_0 \|\mathbf{p}_n - \mathbf{p}_\text{T}\|_2}, \quad (10)$$

$$h_{\text{out},n}(\boldsymbol{\theta}) = \cos^{q_e}(\theta_{\text{el}}) e^{jk_0 \mathbf{p}_n^\top \mathbf{u}(\boldsymbol{\theta})}. \quad (11)$$

2) *Radiation Pattern Calculation Based on (7)*: By replacing the RIS response $\boldsymbol{\Theta}$ with $(\boldsymbol{\Theta}^{-1} - \mathbf{S})^{-1}$ according to (7), the mutual coupling-aware RIS radiation pattern can be computed as

$$E(\boldsymbol{\theta}) = |\mathbf{h}_{\text{out}}^\top(\boldsymbol{\theta}) (\boldsymbol{\Theta}^{-1} - \mathbf{S})^{-1} \mathbf{h}_{\text{in}}|. \quad (12)$$

For clarification, we denote the radiation pattern calculated based on (12) as $E(\boldsymbol{\theta}; \mathbf{S})$, showing it is a function of scattering matrix \mathbf{S} . In contrast, we denote the radiation pattern calculated through (9) as $E(\boldsymbol{\theta}; \mathbf{0})$ for distinction. Besides, antenna radiation patterns are usually normalized with respect to their maximum value, yielding normalized radiation patterns. To do so, we define the normalized version of (9) and (12) as

$$E_n(\boldsymbol{\theta}; \mathbf{0}) = E(\boldsymbol{\theta}; \mathbf{0}) / (\max_{\boldsymbol{\theta}} E(\boldsymbol{\theta}; \mathbf{0})), \quad (13)$$

$$E_n(\boldsymbol{\theta}; \mathbf{S}) = E(\boldsymbol{\theta}; \mathbf{S}) / (\max_{\boldsymbol{\theta}} E(\boldsymbol{\theta}; \mathbf{S})). \quad (14)$$

B. Scattering Parameters Training

Based on the derivation in Section IV-A, we now design a training procedure to estimate the unknown scattering matrix \mathbf{S} based on (12). As mentioned in Section III-B, matrix \mathbf{S} is symmetric, indicating that the degree-of-freedom (DoF) of \mathbf{S} is $N(N+1)/2$. Considering the geometry of the uniform planar array (UPA) of RIS antennas, the DoF of \mathbf{S} can be further reduced.

Typically, introducing a third antenna between two existing antennas will result in an EM interaction characterized by indirect coupling, which is generally exceedingly weak. Moreover, this attenuation intensifies with an increasing number of antennas in between, implying that the mutual coupling between two antennas separated by multiple intervening antennas is negligible. Therefore, in this study, we only consider the mutual coupling between antenna pairs with 0 or 1 intervening antennas, while ignoring the rest, as shown in Fig. 7. Furthermore, we note that the unit cells in our RIS prototype exhibit fold symmetry along the y -axis rather than rotational symmetry. In consideration of such geometric configuration, we can summarize that there are only 8 different values of S-parameters in \mathbf{S} , which we denote as S_1, S_2, \dots, S_8 , as depicted in Fig. 7. Additionally, we denote the self-scattering parameter as S_0 . Hence, we can approximately express the scattering matrix \mathbf{S} as

$$\mathbf{S} \approx \sum_{i=0}^8 S_i \mathbf{A}_i, \quad (15)$$

where \mathbf{A}_i is the known support matrix of the value S_i in \mathbf{S} . Namely, the entry at the j -th row and k -th column is $A_{i,jk} = 1$ for all $S_{jk} = S_i$; otherwise, $A_{i,jk} = 0$. For example, the support matrix for the self-coupling S_0 is $\mathbf{A}_0 = \mathbf{I}_{N^2}$. This expression suggests the DoF of \mathbf{S} is reduced to 9, which is independent of the RIS size N . In other words, the scattering matrix \mathbf{S} can be determined by these 9 parameters $\{S_0, \dots, S_8\}$.

According to (14), the mutual coupling-aware normalized radiation pattern $E_n(\boldsymbol{\theta}; \mathbf{S})$ is a function of \mathbf{S} and thus is a function of parameters $\{S_0, \dots, S_8\}$. We can further denote it as $E_n(\boldsymbol{\theta}; S_0, \dots, S_8)$. Suppose there is a normalized radiation pattern obtained through a 3D full-wave simulation based on the design RIS prototype, denoted as $\bar{E}_n(\boldsymbol{\theta})$. We sample this simulated pattern over AoD $\boldsymbol{\theta}$, thus acquiring the discrete version of the simulated pattern as $\bar{E}_n(\boldsymbol{\theta}_i), i = 1, 2, \dots, N_S$. Here, N_S denotes the number of samples. Then, based on $\bar{E}_n(\boldsymbol{\theta}_i)$, the scattering parameters $\{S_0, \dots, S_8\}$ can be estimated by solving the following minimization problem:

$$\{\hat{S}_0, \dots, \hat{S}_8\} = \arg \min_{S_0, \dots, S_8} \sum_{i=1}^{N_S} (E_n(\boldsymbol{\theta}_i; S_0, \dots, S_8) - \bar{E}_n(\boldsymbol{\theta}_i))^2. \quad (16)$$

Subsequently, the scattering matrix can be recovered as

$$\hat{\mathbf{S}} = \sum_{i=0}^8 \hat{S}_i \mathbf{A}_i. \quad (17)$$

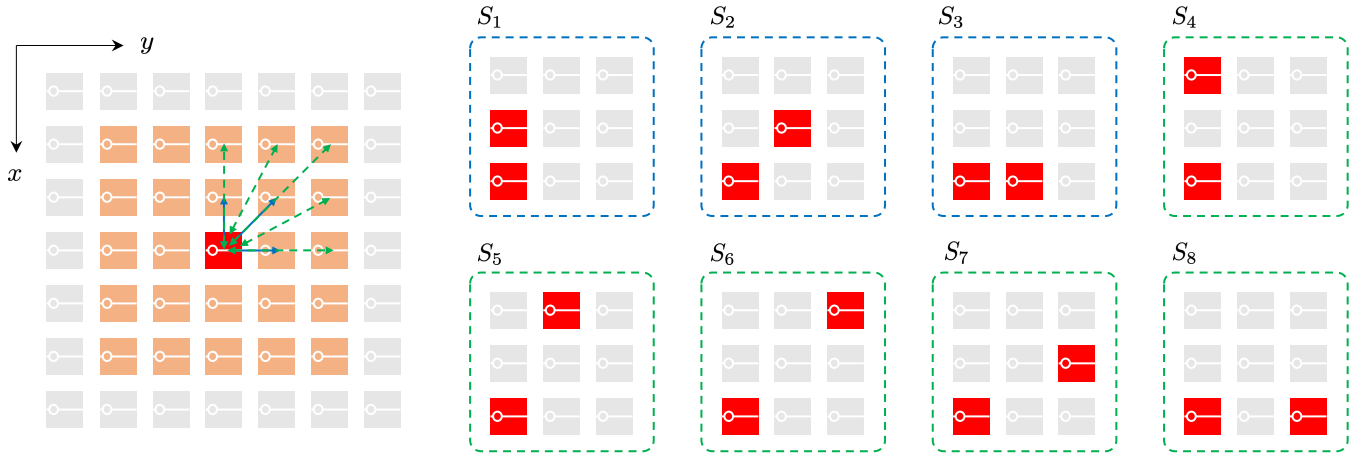


Fig. 7. The illustration of different types of S-parameter based on geometric configurations. For each RIS antenna, we only consider the coupling with its nearest 24 neighboring antennas. As depicted, our RIS unit cells are folded symmetric along the y -axis, but not rotationally symmetric. Therefore, based on geometric relationships, there are only 8 different values of S-parameters in $\tilde{\mathbf{S}}$, which we represent as S_1, S_2, \dots, S_8 , corresponding to the cases shown in the figure. In addition, we use S_0 to denote the self-scattering parameter.

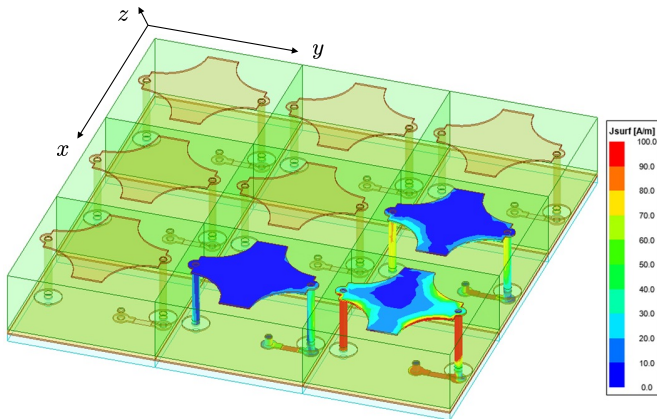


Fig. 8. The simulated antenna model of 3×3 MIMO configuration, where the surface current distributions on the 3 chosen antenna cells are plotted.

V. SIMULATION RESULTS

This section first conducts the model training procedure as described in Section IV-B, and then assesses the accuracy of the trained model via full-wave simulation.

A. Model training

The optimization problem (16) is non-convex due to the modulus operation in (12). Furthermore, the presence of such a modulus operation makes the objective function in (16) non-differentiable, thus the classical gradient-based algorithms are inapplicable.⁵ Although the numerical gradient can be obtained through, e.g., finite difference approximations, an accurate initial estimate close to the true S_0, S_1, \dots, S_8 must be guaranteed to avoid falling into local minima. The following initialization step targets providing such an accurate initial estimate.

⁵Such inverse estimation based on the phaseless observations is also known as the phase retrieval problem [39]–[41].

TABLE I
SIMULATED SCATTERING PARAMETERS IN MIMO CONFIGURATION

Scattering Parameter	Magnitude (dB)	Phase (degree)
\tilde{S}_0	-9.5215	-16.4
\tilde{S}_1	-15.1365	146.8
\tilde{S}_2	-18.9885	54.4
\tilde{S}_3	-19.1683	40.0
\tilde{S}_4	-25.8747	36.5
\tilde{S}_5	-21.5950	6.5
\tilde{S}_6	-28.4459	-142.4
\tilde{S}_7	-24.9849	-107.4
\tilde{S}_8	-25.6949	-84.5

1) *Initialization*: As mentioned in Section IV, the scattering matrix \mathbf{S} for the RIS cannot be measured or simulated directly since RIS is excited through incident EM waves instead of direct feeding ports. Nevertheless, from the EM coupling perspective, the mutual coupling of the reflective RIS antennas and the transmitting MIMO antennas should possess a similar tendency. Hence, a similar antenna model with MIMO configuration can be simulated using commercial full-wave simulation software such as Ansys HFSS, to obtain an approximated scattering matrix to initialize (16). We simulate a 3×3 MIMO antenna array with a similar physical layout as RIS using Ansys HFSS, as presented in Fig. 8.⁶

The simulated results of the scattering parameters among such a MIMO antenna array are listed in Table I. To be clear, we denote these simulated MIMO scattering parameters as $\tilde{S}_0, \tilde{S}_1, \dots, \tilde{S}_8$ and the corresponding scattering matrix as $\tilde{\mathbf{S}} = \sum_{i=0}^8 \tilde{S}_i \mathbf{A}_i$. By observing the data in Table I, insights are obtained that the adjacent coupling in the x -axis direction is stronger than that in the y -axis direction, since $|\tilde{S}_1| > |\tilde{S}_3|$. This phenomenon results from the non-rotational symmetry of

⁶A 3×3 antenna array includes all values of S_0, S_1, \dots, S_8 shown in Fig. 7.

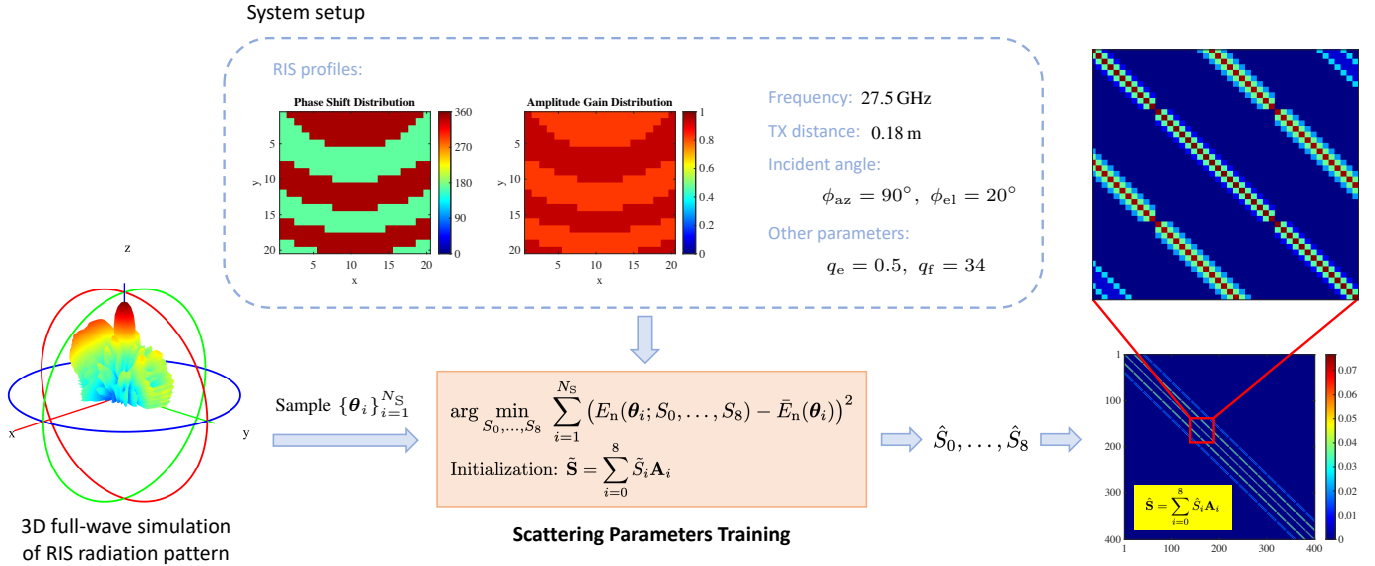


Fig. 9. The scattering parameters training procedure based on a single 3D full-wave simulation of RIS radiation pattern.

TABLE II
ESTIMATED SCATTERING PARAMETERS IN FIG. 9

Scattering Parameter	Magnitude (dB)	Phase (degree)
\hat{S}_0	-11.1596	26.9
\hat{S}_1	-11.3129	110.9
\hat{S}_2	-14.3540	-83.4
\hat{S}_3	-14.5427	-31.8
\hat{S}_4	-22.3376	89.1
\hat{S}_5	-22.2307	-171.3
\hat{S}_6	-15.9014	115.3
\hat{S}_7	-16.8129	98.8
\hat{S}_8	-20.7277	75.6

the antenna structure. To further validate and better understand this difference. The surface current distribution of the MIMO antenna configuration is also demonstrated in Fig. 8. Here, the unit in the right-bottom corner is excited, leading to the induction of currents in neighboring units through the coupling effect. Therefore, the EM coupling along the x and y -axes can be intuitively observed through the surface current distribution on adjacent unit cells. It is clear that the coupling along the x -axis results in a stronger coupled surface current than that along the y -axis, coinciding with the simulated results in Table I. These observations imply that the mutual coupling in the RIS can also exhibit such a trend.

2) *Training Results*: Utilizing the simulated data in Table I as an initialization, the optimization problem (16) can be solved using the gradient descent method with the numerical gradient. The observations $\bar{E}_n(\theta_i)$, $i = 1, 2, \dots, N_S$ are obtained through a single 3D full-wave simulation of RIS radiation pattern using Ansys HFSS. Here, we sample the 3D pattern uniformly such that $N_S = 91 \times 91$. This simulation is conducted at frequency of 27.5 GHz, where the Tx horn is placed at a distance of 0.18 m to the RIS with incident

angle $\phi_{az} = 90^\circ$, $\phi_{el} = 20^\circ$. The RIS phase shifts and amplitude gains are assigned following the beamforming method in [24]. The overall model training procedure and results are visualized in Fig. 9, and the values of the estimated scattering parameters $\hat{S}_0, \hat{S}_1, \dots, \hat{S}_8$ are listed in Table II.

B. Simulation Validation

Since we have learned a scattering matrix $\hat{\mathbf{S}}$ based on the simulated RIS radiation pattern in Fig. 9, we now evaluate the accuracy of the estimated $\hat{\mathbf{S}}$ thus evaluating the accuracy of model (7). We conduct another 3 different full-wave simulations of RIS radiation pattern by varying the system setup. Specifically, we change the incident elevation angle of the Tx horn to $\phi_{el} = 30^\circ, 40^\circ$, and 50° , respectively. The corresponding RIS beamforming is also changing according to the method in [24]. Fig. 10 compares the different theoretical predictions and the full-wave simulation (serving as ground truth) of RIS radiation patterns over these 3 different setups. The evaluated theoretical results include the prediction based on the conventional mutual coupling-unaware model (i.e., $E_n(\theta; \mathbf{0})$), the prediction based on the mutual coupling-aware model using simulated $\hat{\mathbf{S}}$ in the MIMO setup (i.e., $E_n(\theta; \hat{\mathbf{S}})$), and the prediction based on the mutual coupling-aware model using trained $\hat{\mathbf{S}}$ (i.e., $E_n(\theta; \hat{\mathbf{S}})$).

Typically, for the normalized radiation pattern of an antenna array, the predicting accuracy of its sidelobe (especially the strongest sidelobe) is a major concern. As demonstrated in Fig. 10, the prediction based on the mutual coupling-aware model using trained $\hat{\mathbf{S}}$ (red dashed curve) outperforms the other two theoretical predictions, showing the highest accuracy aligned with the full-wave simulations across the three tested setups. The corresponding prediction error is quantified and listed in Table III. Here, the presented prediction error is calculated as

$$\text{PE} = \frac{\|E_n(\theta; \mathbf{S}) - \bar{E}_n(\theta)\|_2}{\|\bar{E}_n(\theta)\|_2}, \quad (18)$$

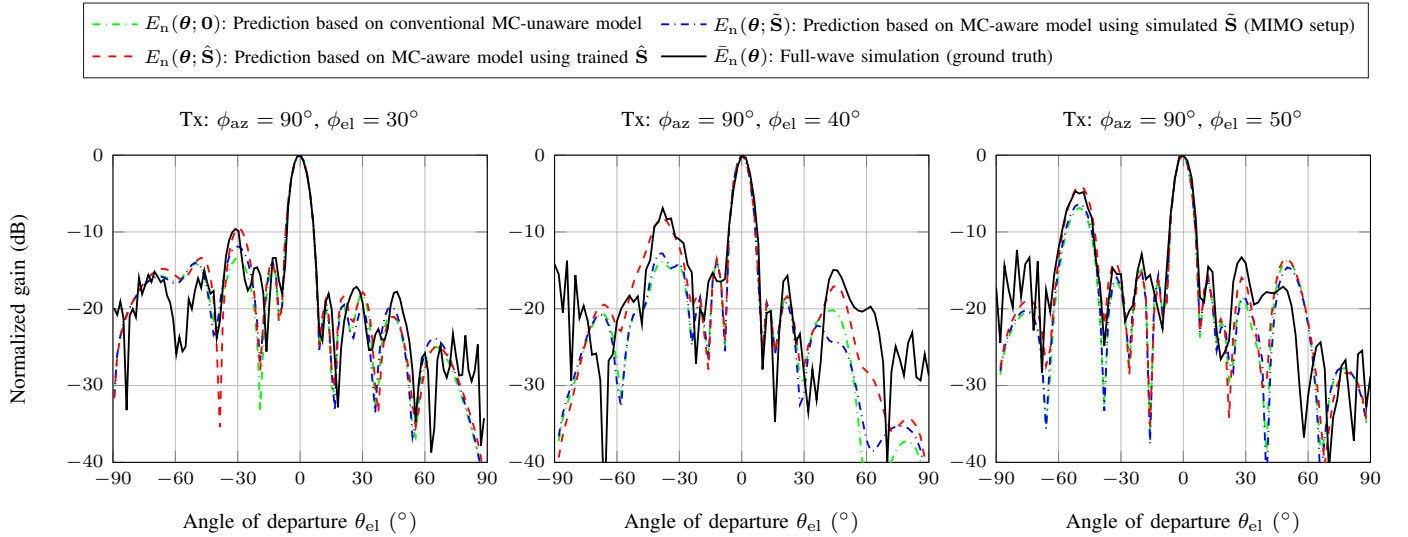


Fig. 10. The comparison of the RIS radiation pattern obtained through the mutual coupling-unaware model, the mutual coupling-aware model using simulated $\tilde{\mathbf{S}}$ (MIMO setup), the mutual coupling-aware model using trained $\hat{\mathbf{S}}$, and the full-wave simulation.

TABLE III
PREDICTION ERROR OF THE RESULTS IN FIG. 10

Incident Angle	$E_n(\theta; \mathbf{0})$	$E_n(\theta; \tilde{\mathbf{S}})$	$E_n(\theta; \hat{\mathbf{S}})$
$\phi_{el} = 30^\circ$	24.7 %	23.8 %	23.5 %
$\phi_{el} = 40^\circ$	44.4 %	39.8 %	33.8 %
$\phi_{el} = 50^\circ$	32.8 %	33.6 %	27.9 %

where $\mathbf{S} = \{\mathbf{0}, \tilde{\mathbf{S}}, \hat{\mathbf{S}}\}$. It is observed that the trained model $E_n(\theta; \hat{\mathbf{S}})$ surpasses the other two models in predicting the RIS radiation pattern with higher accuracy. Particularly, at $\phi_{el} = 40^\circ$, there is a reduction of 10.6% in prediction error observed. These results reveal that: (i) **the mutual coupling-aware communication model (7) can correctly describe the mutual coupling effect in RIS**, thus presenting a more precise performance in predicting RIS radiation pattern compared to the mutual coupling-unaware model $E_n(\theta; \mathbf{0})$. (ii) **the proposed model training method can accurately estimate the scattering matrix \mathbf{S}** , as the prediction result using trained $\hat{\mathbf{S}}$ significantly and consistently outperforms that using simulated $\tilde{\mathbf{S}}$ in MIMO setup.

VI. EXPERIMENTAL RESULTS

Although the accuracy of the mutual coupling-aware model and the trained scattering matrix have been verified by full-wave simulation in Section V-B, further validations are performed in this section through experimental measurement on the fabricated RIS prototype described in Section II-B. The measurement setup is demonstrated in Fig. 11. Here, we use two PE9851B/SF-20 horn antennas to transmit and receive wireless signals, while the fabricated 1-bit quasi-passive RIS is utilized to reflect the EM waves. As mentioned, an MCU WROOM-32 module is used to control the beamforming at the RIS, which can be visualized through the LED array at the back surface of the RIS. Based on this setup, the S-parameter between the Tx and Rx horns can be measured

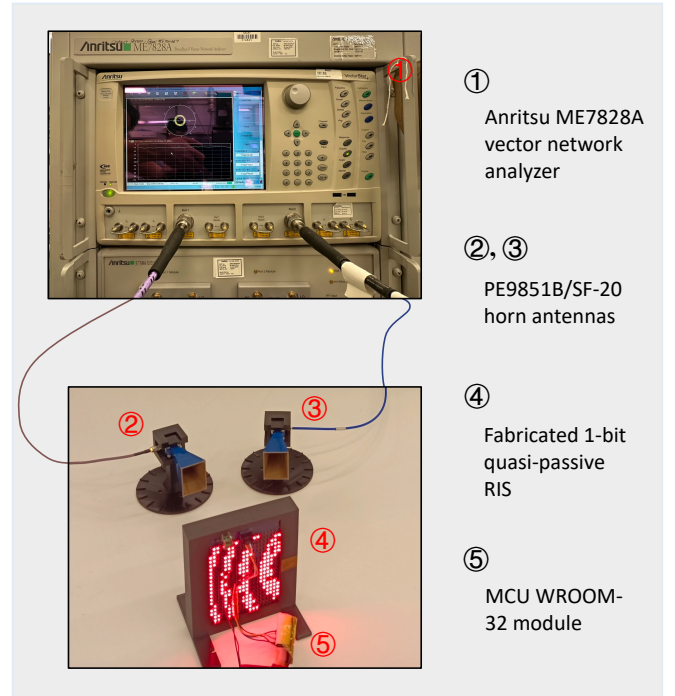


Fig. 11. Experimental measurement setup for the fabricated RIS prototype. The S-parameter between two horns is measured using a vector network analyzer.

using an Anritsu ME7828A vector network analyzer. This real measured Tx-Rx S-parameter is denoted as \bar{S}_{RT} .

On the other hand, both communication model (6) and (7) (with trained $\hat{\mathbf{S}}$) can be adopted to predict this S-parameter S_{RT} . By comparing both theoretical predictions with the measured results, we can assess the precision of model (6) and (7). Specifically, the S-parameter between Tx

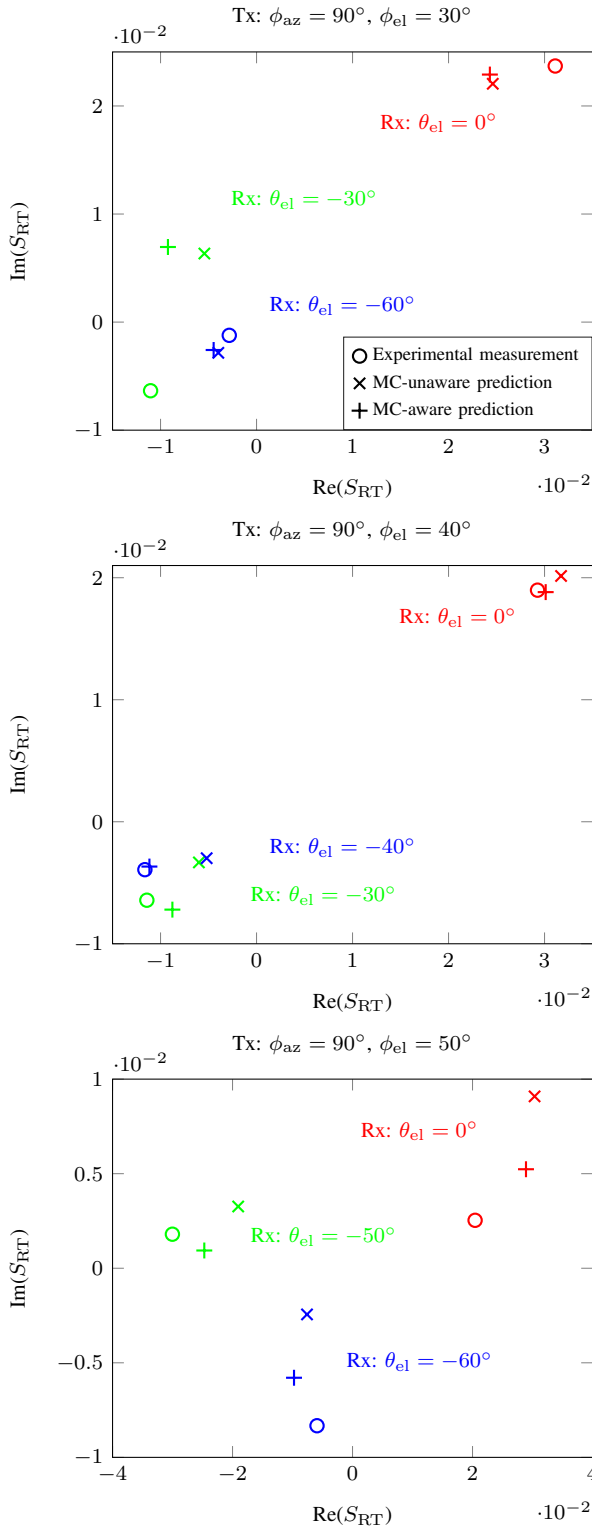


Fig. 12. Comparison of the S_{RT} between Tx and Rx horns obtained by the experiment measurement, MC-unaware prediction, and MC-aware prediction.

and Rx horns can be theoretically calculated as

$$\text{MC-unaware: } S_{RT} = \mathbf{h}_{RI} \mathbf{\Theta} \mathbf{h}_{IT}, \quad (19)$$

$$\text{MC-aware: } S_{RT} = \mathbf{h}_{RI} (\mathbf{\Theta}^{-1} - \hat{\mathbf{S}})^{-1} \mathbf{h}_{IT}. \quad (20)$$

Here, the wireless channels \mathbf{h}_{IT} and \mathbf{h}_{RI} are computed as

$$h_{IT,n} = \frac{\cos^{q_t}(\theta_{T,n})}{\|\mathbf{p}_n - \mathbf{p}_T\|_2^{0.895}} e^{-jk_0 \|\mathbf{p}_n - \mathbf{p}_T\|_2}, \quad (21)$$

$$h_{RI,n} = \frac{\cos^{q_e}(\theta_{e,n}) \cos^{q_t}(\theta_{R,n})}{\|\mathbf{p}_n - \mathbf{p}_R\|_2^{0.895}} e^{-jk_0 \|\mathbf{p}_n - \mathbf{p}_R\|_2}, \quad (22)$$

where \mathbf{p}_T and \mathbf{p}_R stand for the positions of the Tx and Rx horns, respectively. Before the final comparison, we process the following minimization to remove the global phase shift and amplitude loss:

$$\{\hat{\alpha}, \hat{\beta}\} = \arg \min_{\alpha, \beta} \sum_{i=1}^D |\alpha e^{j\beta} S_{RT,i} - \bar{S}_{RT,i}|^2, \quad (23)$$

where i indices the prediction or measurement over different system setups. Finally, we adopt $\hat{\alpha} e^{j\hat{\beta}} S_{RT,i}$, $i = 1, 2, \dots$, as the theoretical prediction for both models.

The measured and predicted S-parameters over different setups are plotted in Fig. 12. Here, the 3 subfigures show the results of 3 different setups of the Tx horn, which correspond to the setups in Fig. 10. For each Tx setup, we test the cases where the Rx horn is placed at the 3 chosen AoDs θ_{el} corresponding to the peak values in Fig. 10, aiming to attain higher SNRs. Both the distance between Tx and RIS and the distance between Rx and RIS are set as 0.18 m. The results in the case of $\phi_{el} = 30^\circ$ seem to indicate that both the mutual coupling-aware and -unaware models exhibit a comparable level of accuracy benchmarked against the real measured results. This can be attributed to that the improvement of the trained model is minor in this case, as shown in Table III. In the cases $\phi_{el} = 40^\circ$ and $\phi_{el} = 50^\circ$, however, we can clearly observe that the mutual coupling-aware predictions are much closer to the measured results compared to the mutual coupling-unaware predictions. This observation again **validates the correctness of the scattering matrix-based model (7) and the accuracy of our estimation on S.**

VII. CONCLUSION

This paper conducts the first realistic evaluation of the mutual coupling in RIS-aided communication based on an authentic RIS prototype. Adopting the scattering matrix-based model, we parameterize the RIS scattering matrix by analyzing the geometric configuration of RIS antennas. A practical training approach for these scattering parameters is proposed leveraging a single 3D full-wave simulation of the RIS radiation pattern. Both full-wave simulations and experimental measurements are carried out to verify the accuracy of the trained model. The results of this work validate the correctness of the RIS-aided wireless communication model based on scattering matrices. Furthermore, it offers an effective method to estimate RIS scattering parameters, foreseeing substantial potential in applications such as RIS-aided channel estimation, beamforming, radio localization, etc.

REFERENCES

- [1] M. Di Renzo, F. H. Danufane, and S. Tretyakov, "Communication models for reconfigurable intelligent surfaces: From surface electromagnetics to wireless networks optimization," *Proceedings of the IEEE*, vol. 110, no. 9, pp. 1164–1209, 2022.

- [2] C. Pan, G. Zhou, K. Zhi, S. Hong, T. Wu, Y. Pan, H. Ren, M. D. Renzo, A. Lee Swindlehurst, R. Zhang, and A. Y. Zhang, "An overview of signal processing techniques for RIS/IRS-aided wireless systems," *IEEE Journal of Selected Topics in Signal Processing*, vol. 16, no. 5, pp. 883–917, 2022.
- [3] X. Pei, H. Yin, L. Tan, L. Cao, Z. Li, K. Wang, K. Zhang, and E. Björnson, "RIS-aided wireless communications: Prototyping, adaptive beamforming, and indoor/outdoor field trials," *IEEE Transactions on Communications*, vol. 69, no. 12, pp. 8627–8640, 2021.
- [4] H. V. Cheng and W. Yu, "Degree-of-freedom of modulating information in the phases of reconfigurable intelligent surface," *IEEE Transactions on Information Theory*, pp. 1–1, 2023.
- [5] E. Björnson, H. Wymeersch, B. Matthiesen, P. Popovski, L. Sanguinetti, and E. de Carvalho, "Reconfigurable intelligent surfaces: A signal processing perspective with wireless applications," *IEEE Signal Processing Magazine*, vol. 39, no. 2, pp. 135–158, 2022.
- [6] X. Song, J. Xu, F. Liu, T. X. Han, and Y. C. Eldar, "Intelligent reflecting surface enabled sensing: Cramér-Rao bound optimization," *IEEE Transactions on Signal Processing*, vol. 71, pp. 2011–2026, 2023.
- [7] P. Zheng, H. Chen, T. Ballal, M. Valkama, H. Wymeersch, and T. Y. Al-Naffouri, "JrCUP: Joint RIS calibration and user positioning for 6G wireless systems," *IEEE Transactions on Wireless Communications (early access)*, 2023.
- [8] H. Chen, P. Zheng, M. F. Keskin, T. Al-Naffouri, and H. Wymeersch, "Multi-RIS-enabled 3D sidelink positioning," *IEEE Transactions on Wireless Communications (early access)*, 2024.
- [9] P. Zheng, X. Liu, J. He, G. Seco-Granados, and T. Y. Al-Naffouri, "LEO satellite and RIS: Two keys to seamless indoor and outdoor localization," *arXiv preprint arXiv:2312.16946*, 2023.
- [10] Z. Wan, Z. Gao, F. Gao, M. D. Renzo, and M.-S. Alouini, "Terahertz massive MIMO with holographic reconfigurable intelligent surfaces," *IEEE Transactions on Communications*, vol. 69, no. 7, pp. 4732–4750, 2021.
- [11] J. Sang, Y. Yuan, W. Tang, Y. Li, X. Li, S. Jin, Q. Cheng, and T. J. Cui, "Coverage enhancement by deploying RIS in 5G commercial mobile networks: Field trials," *IEEE Wireless Communications*, pp. 1–21, 2022.
- [12] Z. Zhang, L. Dai, X. Chen, C. Liu, F. Yang, R. Schober, and H. V. Poor, "Active RIS vs. passive RIS: Which will prevail in 6G?" *IEEE Transactions on Communications*, vol. 71, no. 3, pp. 1707–1725, 2023.
- [13] C. Huang, A. Zappone, G. C. Alexandropoulos, M. Debbah, and C. Yuen, "Reconfigurable intelligent surfaces for energy efficiency in wireless communication," *IEEE Transactions on Wireless Communications*, vol. 18, no. 8, pp. 4157–4170, 2019.
- [14] J. He, H. Wymeersch, and M. Juntti, "Channel estimation for RIS-aided mmWave MIMO systems via atomic norm minimization," *IEEE Transactions on Wireless Communications*, vol. 20, no. 9, pp. 5786–5797, 2021.
- [15] B. Di, H. Zhang, L. Song, Y. Li, Z. Han, and H. V. Poor, "Hybrid beamforming for reconfigurable intelligent surface based multi-user communications: Achievable rates with limited discrete phase shifts," *IEEE Journal on Selected Areas in Communications*, vol. 38, no. 8, pp. 1809–1822, 2020.
- [16] A. Fascista, M. F. Keskin, A. Coluccia, H. Wymeersch, and G. Seco-Granados, "RIS-aided joint localization and synchronization with a single-antenna receiver: Beamforming design and low-complexity estimation," *IEEE Journal of Selected Topics in Signal Processing*, vol. 16, no. 5, pp. 1141–1156, 2022.
- [17] X. Tang, X. Lan, D. Zhai, R. Zhang, and Z. Han, "Securing wireless transmissions with RIS-receiver coordination: Passive beamforming and active jamming," *IEEE Transactions on Vehicular Technology*, vol. 70, no. 6, pp. 6260–6265, 2021.
- [18] G. Gradoni and M. Di Renzo, "End-to-end mutual coupling aware communication model for reconfigurable intelligent surfaces: An electromagnetic-compliant approach based on mutual impedances," *IEEE Wireless Communications Letters*, vol. 10, no. 5, pp. 938–942, 2021.
- [19] M. Di Renzo, V. Galdi, and G. Castaldi, "Modeling the mutual coupling of reconfigurable metasurfaces," in *17th European Conference on Antennas and Propagation (EuCAP)*, 2023.
- [20] X. Qian and M. D. Renzo, "Mutual coupling and unit cell aware optimization for reconfigurable intelligent surfaces," *IEEE Wireless Communications Letters*, vol. 10, no. 6, pp. 1183–1187, 2021.
- [21] A. Abrardo, D. Dardari, M. Di Renzo, and X. Qian, "MIMO interference channels assisted by reconfigurable intelligent surfaces: Mutual coupling aware sum-rate optimization based on a mutual impedance channel model," *IEEE Wireless Communications Letters*, vol. 10, no. 12, pp. 2624–2628, 2021.
- [22] S. Shen, B. Clerckx, and R. Murch, "Modeling and architecture design of reconfigurable intelligent surfaces using scattering parameter network analysis," *IEEE Transactions on Wireless Communications*, vol. 21, no. 2, pp. 1229–1243, 2022.
- [23] H. Li, S. Shen, M. Nerini, M. Di Renzo, and B. Clerckx, "Beyond diagonal reconfigurable intelligent surfaces with mutual coupling: Modeling and optimization," *arXiv preprint arXiv:2310.02708*, 2023.
- [24] R. Wang, Y. Yang, B. Makki, and A. Shamim, "A wideband reconfigurable intelligent surface for 5G millimeter-wave applications," *IEEE Transactions on Antennas and Propagation (early access)*, 2024.
- [25] L. Dai, B. Wang, M. Wang, X. Yang, J. Tan, S. Bi, S. Xu, F. Yang, Z. Chen, M. D. Renzo, C.-B. Chae, and L. Hanzo, "Reconfigurable intelligent surface-based wireless communications: Antenna design, prototyping, and experimental results," *IEEE Access*, vol. 8, pp. 45913–45923, 2020.
- [26] M. A. ElMossallamy, H. Zhang, L. Song, K. G. Seddik, Z. Han, and G. Y. Li, "Reconfigurable intelligent surfaces for wireless communications: Principles, challenges, and opportunities," *IEEE Transactions on Cognitive Communications and Networking*, vol. 6, no. 3, pp. 990–1002, 2020.
- [27] H. Li, S. Shen, and B. Clerckx, "Beyond diagonal reconfigurable intelligent surfaces: From transmitting and reflecting modes to single-, group-, and fully-connected architectures," *IEEE Transactions on Wireless Communications*, vol. 22, no. 4, pp. 2311–2324, 2023.
- [28] D. M. Pozar, *Microwave engineering*. John Wiley & sons, 2011.
- [29] P. Zheng, H. Chen, T. Ballal, H. Wymeersch, and T. Y. Al-Naffouri, "Misspecified Cramér-Rao bound of RIS-aided localization under geometry mismatch," in *IEEE International Conference on Acoustics, Speech and Signal Processing (ICASSP)*, 2023, pp. 1–5.
- [30] J. Rao, Y. Zhang, S. Tang, Z. Li, C.-Y. Chiu, and R. Murch, "An active reconfigurable intelligent surface utilizing phase-reconfigurable reflection amplifiers," *IEEE Transactions on Microwave Theory and Techniques*, vol. 71, no. 7, pp. 3189–3202, 2023.
- [31] F. Amato, C. W. Peterson, B. P. Degnan, and G. D. Durgin, "Tunneling RFID tags for long-range and low-power microwave applications," *IEEE Journal of Radio Frequency Identification*, vol. 2, no. 2, pp. 93–103, 2018.
- [32] Y. Liu, X. Liu, X. Mu, T. Hou, J. Xu, M. Di Renzo, and N. Al-Dhahir, "Reconfigurable intelligent surfaces: Principles and opportunities," *IEEE Communications Surveys & Tutorials*, vol. 23, no. 3, pp. 1546–1577, 2021.
- [33] H. Chen, H. Sarrieddeen, T. Ballal, H. Wymeersch, M.-S. Alouini, and T. Y. Al-Naffouri, "A tutorial on terahertz-band localization for 6G communication systems," *IEEE Communications Surveys & Tutorials*, vol. 24, no. 3, pp. 1780–1815, 2022.
- [34] P. Zheng, X. Ma, and T. Y. Al-Naffouri, "On the impact of mutual coupling on RIS-assisted channel estimation," *arXiv preprint arXiv:2309.04990*, 2023.
- [35] A. Abrardo, A. Toccafondi, and M. Di Renzo, "Design of reconfigurable intelligent surfaces by using S-parameter multiport network theory—optimization and full-wave validation," *arXiv preprint arXiv:2311.06648*, 2023.
- [36] M. Di Renzo and M. D. Migliore, "Electromagnetic signal and information theory—on electromagnetically consistent communication models for the transmission and processing of information," *arXiv preprint arXiv:2311.06661*, 2023.
- [37] C. A. Balanis, *Antenna theory: analysis and design*. John Wiley & sons, 2016.
- [38] P. Nayeri, F. Yang, and A. Z. Elsherbeni, "Reflectarray antennas: theory, designs, and applications," 2018.
- [39] K. Jaganathan, Y. C. Eldar, and B. Hassibi, "Phase retrieval: An overview of recent developments," *Optical Compressive Imaging*, pp. 279–312, 2016.
- [40] T. Goldstein and C. Studer, "PhaseMax: Convex phase retrieval via basis pursuit," *IEEE Transactions on Information Theory*, vol. 64, no. 4, pp. 2675–2689, 2018.
- [41] X. Li, N. Fu, P. Zheng, and L. Qiao, "A compact super resolution phase retrieval method for Fourier measurement," *IEEE Transactions on Instrumentation and Measurement*, vol. 71, pp. 1–15, 2022.